

# Understanding and Improving CNNs with Complex Structure Tensor: A Biometrics Study

Kevin Hernandez-Diaz\*, Josef Bigun, Fernando Alonso-Fernandez

*ISDD Lab, Halmstad University, Kristian IV:s väg 3,  
Halmstad, 30250, Halland, Sweden*

---

## Abstract

Our study provides evidence that CNNs struggle to effectively extract orientation features. We show that the use of Complex Structure Tensor, which contains compact orientation features with certainties, as input to CNNs consistently improves identification accuracy compared to using grayscale inputs alone. Experiments also demonstrated that our inputs, which were provided by mini complex conv-nets, combined with reduced CNN sizes, outperformed full-fledged, prevailing CNN architectures. This suggests that the upfront use of orientation features in CNNs, a strategy seen in mammalian vision, not only mitigates their limitations but also enhances their explainability and relevance to thin-clients. Experiments were done on publicly available data sets comprising periocular images for biometric identification and verification (Close and Open World) using 6 State of the Art CNN architectures. We reduced SOA Equal Error Rate (EER) on the PolyU dataset by 5-26% depending on data and scenario.

---

\*Corresponding author email: kevin.hernandez-diaz@hh.se

## 1. Introduction

Computer Vision (CV) defines texture as a repetitive pattern [1]. Extracting texture features amounts to finding a vector of parameters from subsets of the pattern to uniquely characterize it. Ideally, it is then necessary for the vector to be invariant to translation inside the same texture and different in another [2]. The squared magnitude of Fourier Transform, FT, a.k.a. the power spectrum, of an image is invariant to image translations. Consequently, the power spectrum of local images has been a main source of texture perception studies [3], and texture feature vectors [4][1][5]. Even Convolutional Neural Networks (CNN) are biased towards texture information [6], even showing that some first-layer ImageNet trained CNNs' filters have similar appearance as members of a Gabor filter-bank [7]. Since Hubel and Wiesel's Nobel Prize-winning work, [8], we know that mammalian vision is enabled by cells, each tuned to a unique orientation of translating bars in its visual field, and are upfront in the brain's data flow, at the visual cortex. There exist cell layers that are invariant to translation, with tune-in angles uniformly and densely sampling  $[0 - \pi]$ , like Gabor functions [9] magnitude responses [10].

Texture plays a crucial role in many image-based biometric recognition systems such as the case of fingerprints [11] or iris [12]. In 2009, the authors of [13] showed the potential of the periocular region for biometric recog-

dition. This region encompasses the iris, eyebrows, eyelids, commissures, skin texture, and the general eye’s shape that can be used for recognition. This information-rich area has shown not only to be quite stable but also to provide high performance for soft-biometrics recognition [14]. The periocular area provides flexibility regarding acquisition and occlusion as a middle ground between face and iris recognition. Like its biometric siblings, it has been the target of several texture extraction algorithms for recognition purposes with good performance [15][16].

In this paper, we propose a set of complex mini conv-nets specialized in extracting texture presence and orientation with texture pattern complexity perfectly representable up to the  $n$ -th order moments of the power spectrum [17] in a region to enhance the performance of CNNs. The main contributions of this paper are as follows:

- We show that CNN networks can benefit from compact orientation features as texture features at the input by improving their a) explainability and focus, b) convergence, c) network size, and d) performance.
- We suggest complex Structure Tensors (CST), which is a further generalization of the ordinary Structure Tensor (ST), as a mini conv-net, relying on complex scalar products and complex non-linearities to provide compact inputs to CNNs. The features provided are dense equals of the local power spectrum, including one provided by a full Gabor filter bank, which approximates cell layers of mammalian vision well.

- Our evidence from biometric recognition confirms more explicitly previous indications that SOA CNN networks alone cannot produce orientation features significant for decisions on training data with reasonable size ( $\approx$  ten thousand images).
- Results indicate that the findings above generalize across different CNN architectures and spectra.

## 2. Background and Related Work

This paper uses a method based on the Structure Tensor Theory (ST) [18] as a compact texture orientation descriptor combined with CNNs. The descriptor, explained in detail in Section 3, employs Complex Derivative of Gaussians to extract gradient information and detect the presence and orientation of line patterns. Besides biometrics, STs have been studied and used in numerous applications, including image enhancement, [19], and medical image analysis [20], but also as a fundamental tool in computer vision, to detect and track key-point with [21] or without scale-space [22], to generate dense optical flow, [23], as well as orientation maps [24]. Symmetry descriptors have been used previously in biometric recognition with success, given their resilience to viewpoint or scale changes [25], but their possible contribution has not yet been studied in the context of Deep Learning. Regarding periocular recognition, the works [25] used the presence and orientation of several symmetry patterns at different scales around selected image keypoints for

both periocular and forensic fingerprint recognition, achieving performance comparable to SOA.

Traditional methods like ST [18], LBP [5], HOG [4], and Gabor [9] try to quantify the presence of line patterns in images, specifically their orientations. However, lately, their use has been superseded by CNNs. Even other studies on CNNs show the importance of quantifying orientation. While filtering profiles similar to Gabor filters are observed in the initial layers of CNNs [26][7], such filtering i) lacks systematic uniform orientation tuning and ii) the (non-linear) magnitude processing for translation invariance. This gap may arise from the assumption that all layers in CNNs must be determined by training data, whereas mammalian vision quantifies orientation uniformly up-front and maintains it throughout adult life.

To exploit potential synergies, researchers have tried to create robust models by combining traditional methods and CNNs in different ways. The authors in [27] combined LBP and RGB features with CNNs for face anti-spoofing, increasing performance while reducing the network size. In [15], the authors proposed a double stream CNN that takes RGB ocular images and Orthogonal Combination-Local Binary Coded Pattern (OCLBCP) texture descriptor as inputs, improving recognition performance. In [28], the authors created a new CNN layer called Local Binary Convolution (LCB) as an alternative to convolutional layers. The network, called Local Binary Convolutional Neural Network (LBCNN), performed the same as regular CNNs while reducing network size and learnable parameters between 9 and 169

times.

In [29], the authors used HOG features and CNN to create an efficient pedestrian tracking and reidentification model across multiple camera views. The authors of [30] used handcrafted HOG features, pre-trained CNNs features, and gender information extracted from a shallow network for periocular recognition. The work [31] used a HOG descriptor over spatial and temporal CNNs shallow features for face expression recognition in video.

The work [26] introduced GaborNet, a modified CNN in which the first layer filters are set to fit the Gabor Function by learning Gabor filter parameters instead of filter values directly. They showed that this modified CNN can outperform classic CNN while reducing the number of learnable parameters. The authors of [32] apply a bank of Gabor filters to face images to obtain responses. Each response image was used to train its own CNN network to achieve face classification. In [33], the authors used the output of two consecutive Gabor filters to train a CNN to recognize between seven possible facial emotions. They showed that Gabor outputs can help CNNs achieve better emotion classification and faster convergence. The work [34] showed that using the response of Gabor filters as input of CNNs can improve recognition of soft-biometrics recognition on face images in CNNs and capsule networks.

### 3. Structure Tensor and power spectrum

The Structure Tensor, ST [18], was originally introduced to provide a compact parametrization of the local power spectrum, which provides rich translation invariant features in texture. ST fits the total least square error line to the local spectrum and calculates the best and worst possible errors. Linearly symmetric patterns family in a local patch, those having iso-curves that are parallel, excite ST the most. In Figures 1 a), b) two (local) patches exemplify the family, here defined as real parts of two distinct planar waves,  $A \exp(i\omega_x x + i\omega_y y)$ .

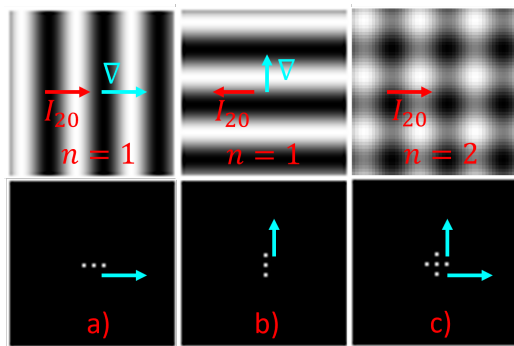


Figure 1: a),b): Examples of 1-folded (linearly) symmetric textures of planar waves with  $I_{20}$  and gradient vectors; c) dito but 2-folded symmetric, with  $n = 2$ . The angle of  $I_{20}$  (red arrows) is twice that of the gradient (blue arrows). FT magnitudes are below.

**ST** is the  $2 \times 2$  symmetric real semipositive definite matrix obtained by averaging the tensor products of image gradients  $\mathbf{ST} = \langle \nabla f \nabla^T f \rangle$  with a filter representing the neighborhood. Its three real elements encode the presence of an oriented texture in the neighborhood.

Satisfying  $\mathbf{ST}u = \lambda u$ , eigenvalues  $0 \leq \lambda_2 \leq \lambda_1$  with corresponding (or-

thogonal) eigenvectors  $u_2$  and  $u_1$  constitute another representation of ST, useful to explain the neighborhood in terms of measurable human observation, texture orientation.

The matrix  $\mathbf{ST}$  can be decomposed as

$$\mathbf{ST} = (\lambda_1 - \lambda_2)u_1u_1^T + \lambda_2(u_1u_1^T + u_2u_2^T) \quad (1)$$

where  $u_1u_1^T + u_2u_2^T = E$  is the unity matrix. Accordingly,  $\mathbf{ST}$  can be uniquely decomposed into an oriented “line” component (encoded by  $u_1u_1^T$ ) with weight-power of  $\lambda_1 - \lambda_2$  and a non-oriented, “balanced”, component (encoded by identity) with the weight-power of  $\lambda_2$ .

If and only if the neighborhood is linearly symmetric, i.e. it possesses texture orientation, its entire spectral power collapses to Dirac distributions located on a line through the (spectral) origin. In the solution, the error of the best fit is  $\lambda_2$  (ideally zero for direction  $u_1$ ), and the worst fit is  $\lambda_1$  (for direction  $u_2$ ). Accordingly, the difference  $\lambda_1 - \lambda_2$  represents the confidence in the fit, whereas  $\theta = \angle u_1$  is the direction of the pattern. However, the confidence is energy dependent, and can vary with the neighborhood contrast.

To exploit the ST theory more effectively, complex numbers can be used to represent the unique decomposition. The main advantage of this “overhaul” is the mathematical completability of STs by power series expansion enabled via the complex representation, allowing to express more elaborate oriented textures, those possessing n-folded symmetries.

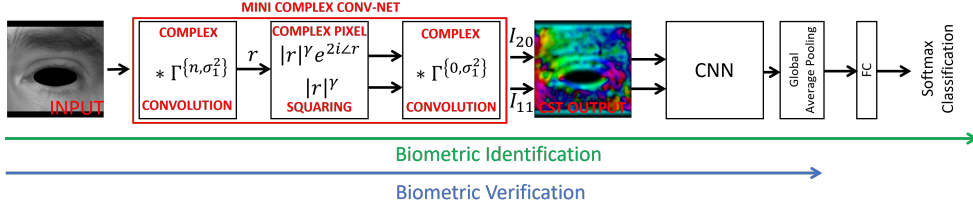


Figure 2: Pipeline of the proposed method.

Complex numbers reduce the unique decomposition (1) to second order complex moments<sup>1</sup> of the neighborhood power spectrum, the complex  $I_{20}$ , and real  $I_{11}$ ,

$$\mathbf{CST} = \left( I_{20}, I_{11} \right) = \left( (\lambda_1 - \lambda_2) \exp(2i\angle u_1), \lambda_1 + \lambda_2 \right) \quad (2)$$

Here  $i = \sqrt{-1}$ , and the **CST** vector has 3 degrees of freedom. Components are readily connected to the unique decomposition of **ST**. The **CST** vector is thus the complex equivalent of **ST**. Replacing the tensor mapping  $u_1 u_1^T$  in 2D, the complex mapping  $2\angle u_1$  is similarly invariant to pattern rotation with  $\pi$  i.e.  $2(\angle u_1 + \pi) = 2\angle u_1$ .

The sum  $\lambda_1 + \lambda_2 = I_{11}$  is a tight upper bound for the confidence  $0 \leq \lambda_1 - \lambda_2 \leq \lambda_1 + \lambda_2$  as  $\lambda_2$  approaches to zero. An exploitable fact is then, that confidence  $|I_{20}|$  equals the upper bound  $I_{11}$  if and only if the pattern possesses texture orientation (=linearly symmetric).

The first benefit is that we can estimate these moments with just 3 separa-

<sup>1</sup> $I_{pq} \triangleq \int (\omega_x + i\omega_y)^p (\omega_x - i\omega_y)^q |F(\omega_x, \omega_y)|^2 d\omega$  where  $F$  is FT of  $f$ .

ble filters, i.e., without a massive filtering process (with a Gabor filter bank), producing the local power spectrum after taking magnitude responses. This is because the axis fitting process is directly available in **CST**. As illustrated by Figure 2, the moments can be obtained directly via a mini-complex convolutional network, comprising convolution of the original image with complex filters given by

$$\Gamma^{\{n,\sigma^2\}}(x,y) = (D_x + iD_y)^n G_{\sigma^2}(x,y) \quad (3)$$

where  $D_x, D_y$  are partial derivatives, and

$$G_{\sigma^2}(x,y) = \frac{1}{2\pi\sigma^2} \exp\left(-\frac{x^2 + y^2}{2\sigma^2}\right), \quad (4)$$

is the familiar Gaussian function with variance  $\sigma^2$ . In the case of texture orientation of linear symmetry type ( $n = 1$ ), the first (linear) box becomes the gradient computation.

The **linear symmetry algorithm** generates elements of **CST**, via three steps each, as follows.

1. Convolve gray image  $f$  with the filter  $\Gamma^{\{n,\sigma^2\}}$ , by setting  $n = 1$ , and  $\sigma = \sigma_1$ . The result is a complex valued image,  $r$ .
2. Square each pixel in  $r$  while emphasizing (gradient) magnitudes with  $\gamma$  to yield two outputs, complex  $r_a = |r|^\gamma \exp(2\angle r)$  having double gradient angles, and real  $r_b = |r|^\gamma$

- 3a Convolve the  $r_a$  strand of Step 2 with the Gaussian filter  $\Gamma^{\{n,\sigma^2\}}$  where  $n = 0$ , and  $\sigma = \sigma_2$  to provide the complex  $I_{20}$ .
- 3b Convolve the  $r_b$  strand of Step 2 with the same Gaussian filter to output the real  $I_{11}$ .

Textures with unique orientation have their 2D power spectra concentrated into a line, as illustrated in Figure 1 a), b). However, multiple orientations can occur in textures such as repeated squarish patterns, as exemplified by Figure 1 c), which will then produce a cross-like pattern in the power spectrum. This makes  $I_{20}$  with  $n = 1$  insufficient, requiring more sophisticated models of orientation presence.

The texture model represented in the above algorithm can then be completed in the mathematical sense by increasing  $n$  to  $n = 2$  in the first box, [17]. This changes only the used filter in the box to  $\Gamma^{\{2,\sigma^2\}}$ , (3), and the same algorithm will instead compute elements of the vector  $(I_{2n,0}, I_{n,n})$ , completing the descriptive ability of lower "n"s. Such increases yield even orders of complex moments of the (local or Gabor) power spectrum, which is even, to quantify its *n-folded symmetry* concentration. Instead of 1 axis as in  $n = 1$ , each  $(I_{2n,0}, I_{n,n})$  pair fits  $n$  evenly distributed axes through the origin. The orientation delivered in  $I_{2n,0}$  is texture group orientation, e.g., how many radians the lines of a squarish pattern deviate from a reference direction.

Using **CST**, we present evidence that CNNs are not able to reach the valuable information embedded in texture orientations. Likewise, the evidence supports that if the orientation of power spectrum concentrations is

extracted and presented to CNNs via complex moments, then they can make decisions with improved accuracy.

#### 4. Methodology

We follow the pipeline shown in Figure 2 to introduce the CST into CNN architectures. The  $\sigma_1$  of the first step determines the frequency band in which CST acts, whereas  $\sigma_2$  in the third step determines neighborhood size. Figure 3 a) shows the effect of using different  $\sigma$  values. Preliminary results showed us that the highest frequencies in our datasets contained the most discriminative information. The neighborhood size only influenced methods where alignment was an issue. We settled therefore for a value for  $\sigma_1$  of 0.6 to extract high-frequency gradients and  $\sigma_2$  of 4.0 to define minimum neighborhood size. Furthermore, we set  $\gamma$  to 0.1 to alleviate the difference in magnitudes between the regions with subtle and fast changes. Figure 3 b) shows the type of texture extracted according to different values of  $n$  and  $\gamma$  for the selected  $\sigma_1$  and  $\sigma_2$ .

To corroborate conclusions, we carried out biometric recognition experiments by six widely used CNN architectures: ResNet50 [35], DenseNet121 [36], Xception [37], InceptionV3 [38], MobileNetV2 [39].

We used Tensorflow-Keras as our Deep Learning framework to download, initialize, train, and test the models. The CST process was transparent to the network and not affected by the training process. We use the standard models provided by the Keras library, only changing the last fully connected layer

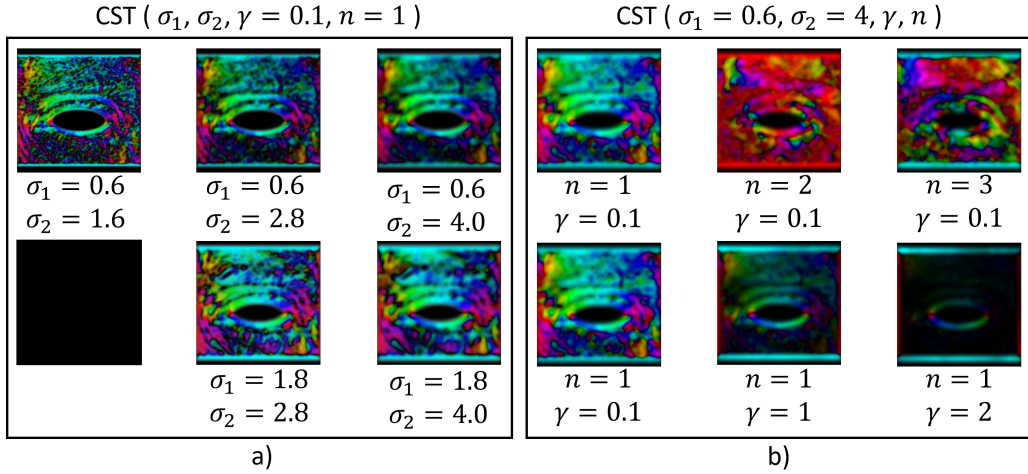


Figure 3: Effect of hyperparameters in the CST output, shown in HSV-colors where Hue is modulated by  $\angle I_{20}$  (i.e.  $0^\circ$  is mapped to red), saturation by  $I_{11}$ , and Value by  $|I_{20}|$ . When the latter two are high (vivid colors), certainty is high.

to fit the number of users in the database and the input size to fit the type of data used. We trained the networks using Stochastic Gradient Descent with a learning rate of 0.001 and a momentum of 0.9. The networks were trained for 100 epochs with a batch size of 16. No data augmentation was used during training. Model checkpoint was used to monitor the validation loss and recover the best-performing version after training. All training was conducted on a Windows 10 machine with an i7-8700, 32GB of RAM, and an Nvidia Titan V.

Database	Protocol	Images (Classes)	Train Partition Images (Classes)	Gen./Imp.Pairs	Test Partition Images (Classes)	Gen./Imp.Pairs
PolyU	5-fold	6,270 (418)	5,016 (418)	-	1,254 (418)	-
	CW		4,180 (418)	18,810/8,715,300	2,090 (418)	4,180/2,178,825
	OW		3,135 (209)	21,945/4,890,600	3,135 (209)	2,1945/4,890,600
Cross-Eyed	5-fold	1920 (240)	*1,680/1,440 (240)	-	*240/480 (240)	-
	CW		1,200 (240)	2,400/717,000	720 (240)	720/258,120
	OW		960 (120)	3,360/456,960	960 (120)	3,360/456,960

Table 1: Summary of Train/Test partitions per database, spectrum, and protocol for the verification experiments, Both databases contain the same number of images in each spectrum. The Close-World (CW) and Open-World (OW) protocols with PolyU and Cross-Eyed are defined following [40]. \*The values indicate the number of images when the test fold is composed of 1 or 2 images per class due to the number of images per user not being divisible by 5.

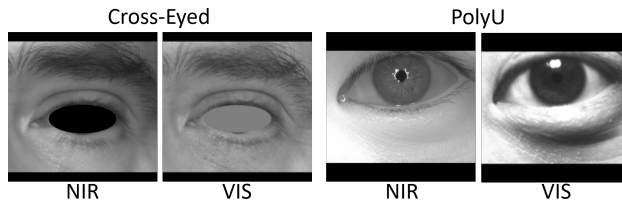


Figure 4: Example images from the databases employed.

## 5. Databases, Metrics, and Protocol

### 5.1. Databases

We employed two commonly used periocular datasets in the experimentation: Cross-Eyed [41], and PolyU [42]. Figure 4 shows some examples of each database.

The **Cross-Eyed** dataset is a cross-spectral periocular database that offers Near-Infrared (NIR) and Visible (VIS) images from subjects of different nationalities, ethnicities, and eye colors using a custom dual-spectrum image sensor under normal indoor illumination. The database contains 8 images of each eye from 120 subjects per spectrum, for a total of 3,840 images. Images were normalized to have the same sclera radius, center, orientation, size, and

dimensions.

The **PolyU** database is a bi-spectral iris database captured using simultaneous bi-spectral imaging by the Hong Kong Polytechnic University. It provides images in NIR and VIS, captured simultaneously, offering exact pixel correspondence between both spectral image versions. The database consists of 15 instances for each spectrum of both eyes of 209 different subjects for a total of 12,540 iris images. Since the periocular region in this dataset is smaller, images are zero-padded to be square while maintaining the aspect ratio.

### *5.2. Metrics and Protocol*

To evaluate the performance of the proposed system, we carried out both biometric identification and verification experiments. For the identification cases, we did 5-fold cross-validation and tested across all user samples using softmax and cross-entropy loss. We performed biometric verification to frame our methods across the SOA results for the used databases. We followed the same protocols as in [40]: the Close-World (CW) protocol, in which the training and test partition contains images of all users without overlap, and the Open-World (OW) protocol, in which the users are split into training and testing along with all their images. The networks used for biometric verification were previously trained for identification using the same training and validation partitions. For testing, we extracted the features from the second to last layer and compared them using the cosine similarity.

## 6. Results and Discussion

### 6.1. Effect of CST input variables

	Input					Cross-Eyed		PolyU		
	BW	$ I_{20} $	$\angle I_{20}$	$\Re(I_{20})$	$\Im(I_{20})$	$I_{11}$	NIR	VIS	NIR	VIS
1 <sup>st</sup>	X						97.8	97.7	93.2	94.5
2 <sup>nd</sup>		X					96.4	97.1	93.7	94.3
3 <sup>rd</sup>		X				X	97.6	97.6	94.7	95.4
4 <sup>th</sup>		X	X			X	98.4	98.4	95.6	96.1
5 <sup>th</sup>				X	X		98.2	98.5	96.0	96.0
6 <sup>th</sup>				X	X	X	98.5	98.6	96.3	<b>96.4</b>
7 <sup>th</sup>		X		X	X	X	98.4	<b>98.7</b>	<b>96.5</b>	<b>96.4</b>
8 <sup>th</sup>	X			X	X	X	<b>98.6</b>	98.2	<b>96.5</b>	96.2
9 <sup>th</sup>	X	X		X	X	X	98.3	98.3	<b>96.5</b>	96.2

Table 2: Average test accuracy from the 5-fold cross-validation identification experiments with respect to the variable type used at the input of a randomly initialized ResNet50.

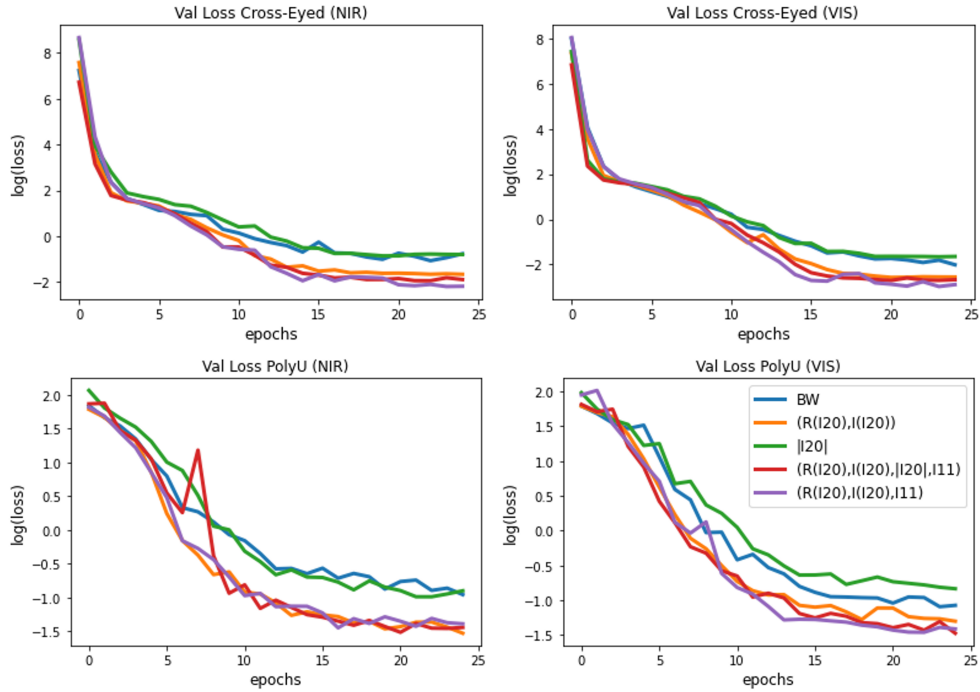


Figure 5: Validation loss during training for a randomly initialized ResNet50 network using different input data.

The first step in our experimentation was to investigate how the representation and presence of  $I_{20}$  and  $I_{11}$  affected the training and performance of the network. Since  $I_{20}$  is complex, we can use either the real  $\Re(I_{20})$  and imaginary  $\Im(I_{20})$  representation or the polar coordinates  $|I_{20}|$  and  $\angle(I_{20})$ . The network input was modified by concatenating the selected representation through the channel axis. Table 2 presents the identification accuracy results for these experiments. Additionally, Figure 5 shows the validation loss during the training process.

From Table 2, we can see that the incremental improvement observed with the addition of each component in the polar coordinates indicates that magnitude, angle, and upper fitting boundary all contain beneficial information offering comparable or better performance than the original grayscale image. Furthermore, the angle information (fourth row) improves the accuracy further for all cases, outperforming the grayscale version for both datasets. This shows that the network can benefit from the orientation information upfront, even if the angle is discontinuous at  $0/360$  degrees in the polar representation. Providing the real and imaginary parts of  $I_{20}$  alone, which also implicitly encodes magnitude and angle, gives similar or better results than the polar counterparts, plus  $I_{11}$ . The addition of  $I_{11}$  to this new case (sixth row) gives extra improvement, highlighting the valuable contribution of all elements in either representation. We also have studied the combination of the original grayscale image with the best variants of the CST representation (8th and 9th row). While also providing the grayscale image can help improve the

accuracy, this may not hold true for all the options (sixth vs. ninth row). The best overall results are obtained with the real and imaginary parts,  $|I_{20}|$ , and  $I_{11}$  (seventh row). This case provides not only direct information on the presence of the linear pattern in the area, but the orientation information is also provided by the real and imaginary values. Another consideration of these results is that our observations hold for the two databases and the two spectra, indicating the generalization capabilities of the proposed method.

We then analyze the benefits of the proposed methods during network training (Figure 5). We do so for selected cases in Table 2. We can observe that just providing the real and imaginary parts already allows for faster convergence and lower loss than when using the grayscale version. However, as with the results in Table 2, providing just the magnitude  $|I_{20}|$  is insufficient to observe tangible benefits. Again, the best case overall corresponds with the addition of  $I_{11}$  and  $|I_{20}|$  to  $I_{20}$ , which can be observed regardless of the database and spectrum employed.

### 6.2. Effect of CST derivative order

Input				Cross-Eyed		PolyU	
BW	$\Gamma\{1,\sigma_1^2\}$	$\Gamma\{2,\sigma_1^2\}$	$\Gamma\{3,\sigma_1^2\}$	NIR	VIS	NIR	VIS
<b>X</b>				97.8	97.7	93.3	94.5
	<b>X</b>			98.6	98.3	95.9	96.4
		<b>X</b>		98.0	97.7	95.8	95.5
			<b>X</b>	97.3	96.6	93.7	94.0
	<b>X</b>	<b>X</b>		98.2	98.4	96.0	95.7
	<b>X</b>	<b>X</b>	<b>X</b>	98.0	98.5	95.9	96.0

Table 3: Average test accuracy for each combination of the Complex Derivative of Gaussian order  $n$ . The complex data representation used at the input is  $\Re(I_{20}), \Im(I_{20}), I_{11}$ .

Another relevant parameter related to the network’s input is how the symmetry order ( $n$  in Equation 3) affects the network. The higher the order, the more intricate texture orientation the model will extract (Figure 3). However, the presence of highly complex patterns is dataset and application dependent. Nonetheless, higher-order symmetries still have some response, making an interesting case for the selection of the input data. In this paper, we experiment with values of  $n$  from 1 to 3. For simplicity, for each value of  $n$ , we use the input combination consisting of  $\Re(I_{20})$ ,  $\Im(I_{20})$ , and  $I_{11}$ . Table 3 shows the results of these experiments. We can see that when only one is used, the first-order derivative of Gaussian ( $n = 1$ ) performs the best, although the second-order still matches or improves the grayscale version. In general, the performance decreases as we increase  $n$ . This is an indication that classes could be separated already by low-order orientation quantification. Even though combining different orders improved the accuracy in some database/method combinations, the effect was not consistently observable.

### 6.3. *Effect of network compression*

Since ready-to-use features are provided up-front, there is potential for network compression and speed improvement. Thus, we also experimented with different network depths, widths, and input resolutions. A coefficient  $\alpha$  was used to reduce the number of filters per layer (width) of ResNet50 with values (0.2, 0.4, 0.6, 0.8, and 1.0), being 1.0 the standard network size. In addition, the input image size was reduced by one-fourth each time while

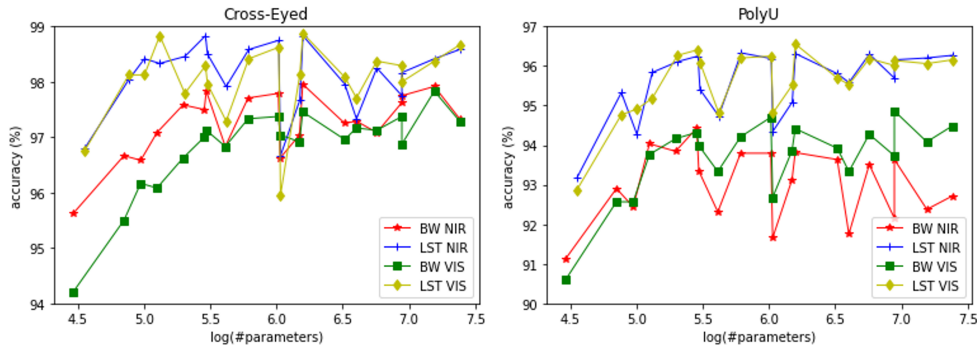


Figure 6: Average test accuracy for different network compression levels. The number of parameters depends on the width of the network, controlled by coefficient  $\alpha$ , and the depth of the network, as explained in Section 6.3. The complex data representation used at the input is  $\Re(I_{20}), \Im(I_{20}), I_{11}$ .

simultaneously changing the network depth to compensate, going from an input size of 256x256 pixels to 32x32 pixels in its shallowest version. We maintained the network’s abstraction level and output resolution by decreasing the depth of the network accordingly.

Figure 6 shows the effect that the amount of parameters has on performance. The amount of parameters depends on the network’s width and depth of the network. The first thing to notice is that all curves exhibit very similar behavior regardless of the database, spectrum, and input type. The slight offset in terms of the number of parameters in comparison to grayscale images is due to the increase in the number of channels at the input. This offset (6,272 parameters) is minor compared to the number of parameters of the original ResNet50 (25.5 million). It can also be seen that CST outperforms the grayscale images in all cases, except for one point in the Cross-Eyed dataset and VIS spectrum at around 1 million parameters.

At this point, the network depth is at its maximum, but the width is at its minimum ( $\alpha = 0.2$ ). Such extreme imbalance is the explanation for the sudden drop in performance observed in the graphs for both datasets. Another observation from the graphs is that the network can go through compression to a large extent without loss in performance, with our solution systematically providing better accuracy for any compression level. This suggests that our method could support compression, producing smaller networks while still benefiting from an increase in performance.

#### 6.4. Consistency across other CNN architectures

Network	Cross-Eyed				PolyU			
	NIR		VIS		NIR		VIS	
	BW	CST	BW	CST	BW	CST	BW	CST
ResNet50	97.8	<b>98.5</b>	97.7	<b>98.6</b>	93.3	<b>96.3</b>	94.5	<b>96.4</b>
DenseNet121	98.3	<b>99.1</b>	97.8	<b>99.3</b>	95.8	<b>98.1</b>	97.2	<b>98.0</b>
Xception	98.5	<b>99.3</b>	98.9	<b>99.6</b>	96.2	<b>98.0</b>	97.4	<b>98.1</b>
InceptionV3	97.8	<b>98.9</b>	97.9	<b>98.3</b>	93.8	<b>96.5</b>	94.9	<b>95.9</b>
MobileNetV2	98.6	<b>99.0</b>	98.4	<b>99.2</b>	94.5	<b>97.3</b>	96.1	<b>97.4</b>

Table 4: Average test accuracy for each network. The complex data representation used at the input is  $\Re(I_{20}), \Im(I_{20}), I_{11}$ . The bold numbers indicate the best case among BW (grayscale images) and CST (our approach). The gray cells indicate the best result per column.

We have also applied the proposed method to other popular CNN architectures to corroborate its benefits. Table 4 shows the results of such experimentation. It can be seen that for all networks and databases, our complex structure tensor version outperforms the baseline grayscale version. For the Cross-Eyed database. For PolyU, our ResNet50 network improves the baseline results by 3.3% for the NIR case and 1.9% for VIS. It is also worth noting the improvements of InceptionV3 and MobileNetV2 with PolyU-NIR

(2.7% and 2.8%, respectively). In absolute terms, the best-performing network for both the baseline and our method is Xception, reaching up to 99, 6% accuracy for the VIS Cross-Eyed data and 98% – 99% accuracy in all other cases. In summary, the observed accuracy improvements with our solution demonstrate that it also generalizes to other CNN architectures.

### 6.5. Performance comparison with previous studies

Table 5 summarizes and compares our results with previous works using the same databases [16][40]. The whole performance for each system can be seen in the ROC curves presented in Figures 7 and 8 for the Close-World and Open-World cases, respectively. This sub-section follows the same protocol as those previous works to enable the comparison as explained in Section 5.2. The CST method in these experiments used the input combination of BW,  $\Re(I_{20}), \Im(I_{20}), I_{11}$ . Including the grayscale image in these experiments proposes a more general approach of using CST with Deep Learning.

		Cross-Eyed (CW)		PolyU (CW)		Cross-Eyed (OW)		PolyU (OW)	
		NIR	VIS	NIR	VIS	NIR	VIS	NIR	VIS
ResNet50	BW	3.7	2.6	1.8	1.3	4.5	<b>2.9</b>	6.4	5.7
	CST	4.6	4.3	1.3	1.3	4.3	4.2	4.9	6.2
	[40]	<b>1.8</b>	1.7	0.68	0.61	3.5	3.4	4.00	<b>3.94</b>
	[16]	-	<b>1.3</b>	-	3.4	-	<b>1.2</b>	-	7.76
Xception	BW	3.5	2.8	0.7	0.6	3.8	3.2	4.7	<b>4.1</b>
	CST	<b>2.2</b>	2.9	0.8	0.6	3.5	4.2	<b>3.8</b>	4.5
DenseNet121	BW	2.8	<b>2.1</b>	0.8	0.8	<b>3.3</b>	3.4	5.4	4.9
	CST	3.9	3.2	<b>0.5</b>	<b>0.5</b>	4.1	3.6	4.8	5.0
	[16]	-	1.6	-	2.49	-	1.7	-	5.82

Table 5: CNN networks comparison with absence and presence of CST input, as well as SOA EERs for each database and spectrum. Bold cells show the best-overall and our best result for each particular setting (column). Shaded cells emphasize improvement with the presence of the CST over using only grayscale images.

In this case, results are more mixed than in the previous subsections.

In particular, the CST approach does not outperform the use of original grayscale images in all cases. This contrast can be partially attributed to the use of 5-fold cross-validation in the previous sections, which shows a more reliable indication of the performance of the system by testing over the whole dataset. This effect mostly happens with the Cross-Eyed database. We attribute this to the more limited training data available in Cross-Eyed since the networks are trained from scratch, and our CST approach involves a higher amount of input channels. Conversely, with PolyU, our approach works better or the same as the original grayscale images in most cases.

From the ROC curves in Figures 7 and 8, one can see that in some cases, despite a higher EER in Table 5, the performance favors ConvNet models using CST information when ROC curves enter the low FAR area. Such cases are the Xception network on the PolyU dataset for both the NIR case and Close-World Protocol, as well as for the VIS spectrum in the Open-World Protocol.

For the Open-World case, our CST model performs better at a lower FAR for every case, with the exception of PolyU in the VIS spectrum, where the difference between models is negligible. For DenseNet121, the performance difference in Cross-Eyed and NIR for the Close-World setting becomes smaller at lower FAR. Despite the variability in the results due to single-partition testing, ROC curve results confirm predictions of the identification sections. Texture orientation information brings measurable performance benefits in recognition compared to using only grayscale information when

networks were not pre-trained at all.

The results of Table 5 indicate the EER of CST and the SOA results from previous studies [16][40] in the same protocol. Despite CST having no access to pre-training, it is able to deliver SOA performance with Xception and DenseNet121 networks in PolyU in CW (both spectra) and in the difficult OW with PolyU in NIR. In the case of ResNet50, which delivers the best performance of state-of-the-art in the protocol, CST was able to come closer than 1 percentage point to the state-of-the-art in CW, PolyU NIR CW, and in the difficult OW PolyU NIR cases. In other cases, CST was lagging behind by not more than 2-3 percentage points. The method of [40] used a ResNet50 network pre-trained for face recognition on the very large VGGFace2 and MS1M databases. This leads us to hypothesize that our strategy of using mini complex ConvNets to complement grayscale with texture orientation at the input of CNNs could also benefit from pre-training on other modalities, such as face, where much larger databases exist. On the other hand, the method of [16] underwent an exhaustive search to find layers of the networks that could provide enhanced verification performance.

## 7. Conclusions

This study examined the benefits of the Complex Structure Tensor theory to improve CNNs by providing measurements representing the presence of unique texture orientation and its angle at the input. We investigated the effect of changing the input image of the network from the original grayscale

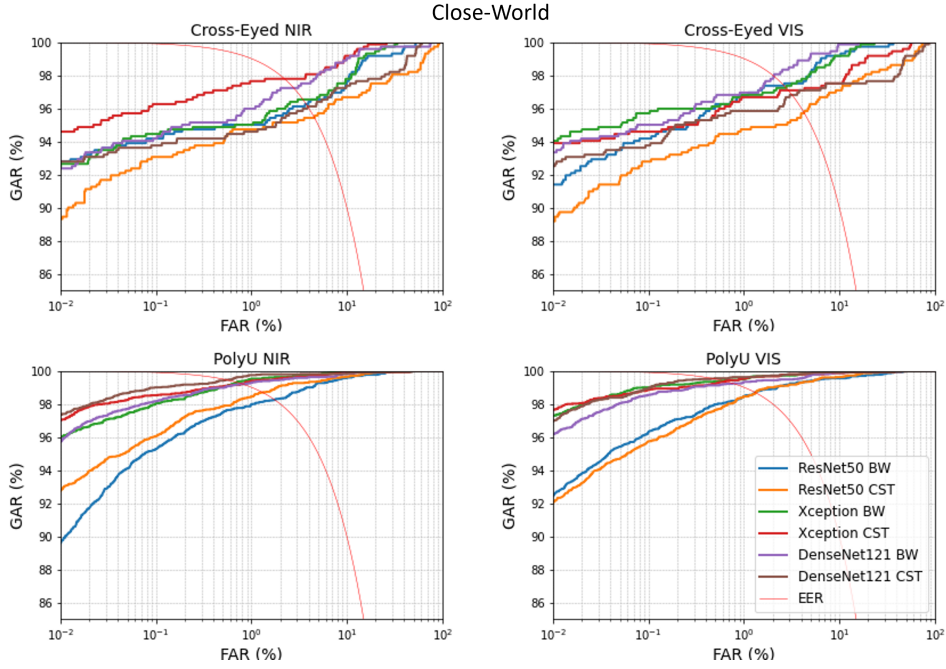


Figure 7: ROC curves for the Close-World setting. The EER values and comparison with the SOA results are given in Table 5

to a preprocessed image where the joint presence of up to  $n$  orientations in the pixels' neighborhood is highlighted. This is achieved via second-order complex moments of local power spectra, which produce a complex-value representation of the image that encodes both the magnitude and angle of the dominant texture (group) orientations. We used periocular recognition as a case study and six well-known network architectures. We employed two common datasets used in periocular research, Cross-Eyed and PolyU, which contain images both in near-infrared (NIR) and visible (VIS) spectra. This allowed us to explore the applicability of our findings to different spectra.

Typically a Gabor filter bank representing the local spectrum is obtained

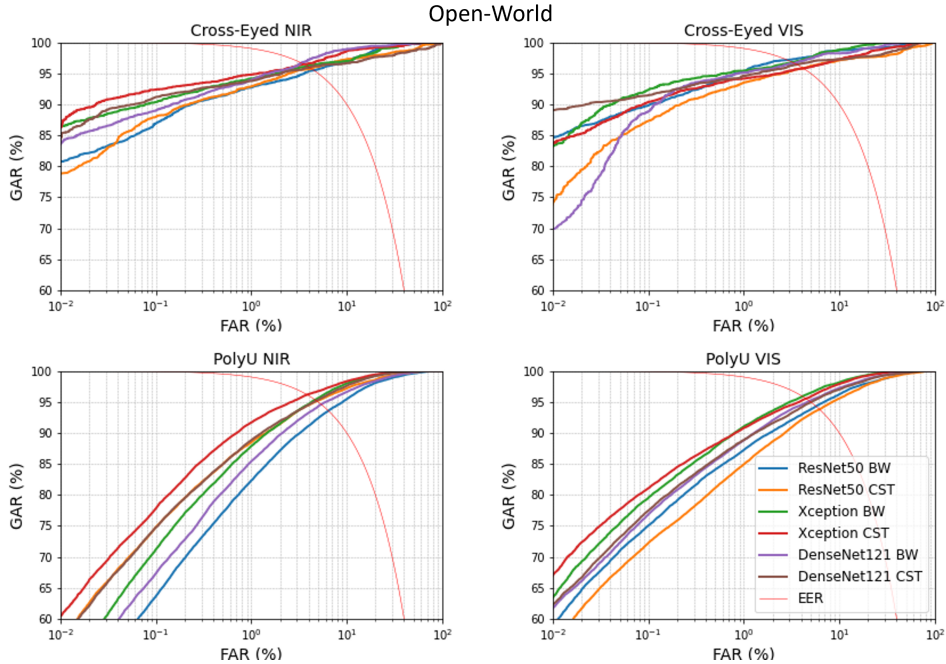


Figure 8: ROC curves for the Open-World setting. The EER values and comparison with the SOA results are given in Table 5

by using 30-100 (=dimension) different filters. In our method, we extract single frequency band texture components in the image, which are then averaged over a neighborhood (configurable via two parameters,  $\sigma_1$  and  $\sigma_2$ , respectively). This approach compresses the feature space dimension of the image that is provided to the network while maintaining translation invariant information of the local power-spectra, improving accuracy and convergence. Improvement is observed regardless of the database, spectrum, or network architecture. This suggests that standard CNNs are not able to effectively reach these features from the gray-scale images, especially when training data is limited.

We show that, with our method, thanks to the reduction of the feature space, network compression is possible while maintaining superior performance. In terms of comparison with prior studies, our method is shown to improve the verification performance when sufficient training data is available.

With orientation features at the input, we also gained explainability as to CNNs’ decision basis. Networks can then focus on what has proven helpful for mammalian vision upfront. Even if CNNs have been shown to extract select texture orientations in first layers, [26][7], our results indicate that providing them upfront reduced the burden of learning and extracting them with higher mathematical systemacy, at no cost (downsizable network). The systemacy included [2] mathematical completeness, interpolative direction, independence of filter bank size for direction accuracy, certainty measure, and translation invariance within textures.

To fully leverage the presented method’s benefits, we aim to go further by making the hyperparameters of the employed filters learnable. Our use of local texture features and the increase in convergence, network compression, and the separability of the filters used, make our model an interesting case for newer architectures like hybrid vision transformers, where recent works focus on models’ accuracy-latency trade-off [43]. Future work also includes applications in CV where texture information and/or certainty play important roles, such as image segmentation [44], or image generation [45].

## 8. Acknowledgements

This work was supported by Vetenskapsrådet [grant numbers 2016-03497 and 2021-05110] and VINNOVA [grant number 2022-00919].

## References

- [1] M. Tuceryan, A. K. Jain, Texture analysis, Handbook of pattern recognition and computer vision (1993) 235–276.
- [2] J. Zhang, T. Tan, Brief review of invariant texture analysis methods, Pattern recognition 35 (3) (2002) 735–747.
- [3] B. Julesz, J. Bergen, Textons, the fundamental elements in preattentive vision and perception of textures, The bell system technical journal 62 (6) (1983) 1619–1645,
- [4] N. Dalal, B. Triggs, Histograms of oriented gradients for human detection, in: 2005 IEEE computer society conference on computer vision and pattern recognition (CVPR'05), Vol. 1, Ieee, 2005, pp. 886–893.
- [5] T. Ojala, M. Pietikainen, D. Harwood, Performance evaluation of texture measures with classification based on kullback discrimination of distributions, in: Proceedings of 12th international conference on pattern recognition, Vol. 1, IEEE, 1994, pp. 582–585.
- [6] R. Geirhos, P. Rubisch, C. Michaelis, M. Bethge, F. A. Wichmann, W. Brendel, Imagenet-trained CNNs are biased towards texture; in-

- creasing shape bias improves accuracy and robustness., in: International Conference on Learning Representations, 2019.
- [7] A. Krizhevsky, I. Sutskever, G. E. Hinton, Imagenet classification with deep convolutional neural networks, *Advances in neural information processing systems* 25 (2012).
- [8] D. Hubel, T. Wiesel, Receptive fields of single neurons in the cat's striate cortex, *J. physiol. (London)* 148 (1959) 574–591.
- [9] G. H. Granlund, In search of a general picture processing operator, *Computer Graphics and Image Processing* 8 (2) (1978) 155–173.
- [10] J. Kulikowski, P. Bishop, Fourier analysis and spatial representation in the visual cortex, *Experientia* 37 (1981) 160–162.
- [11] A. Jain, A. Ross, S. Prabhakar, Fingerprint matching using minutiae and texture features, in: *Proceedings 2001 International Conference on Image Processing (Cat. No. 01CH37205)*, Vol. 3, IEEE, 2001, pp. 282–285.
- [12] J. Daugman, How iris recognition works, in: *The essential guide to image processing*, Elsevier, 2009, pp. 715–739.
- [13] U. Park, A. Ross, A. K. Jain, Periocular biometrics in the visible spectrum: A feasibility study, in: *2009 IEEE 3rd international conference on biometrics: theory, applications, and systems*, IEEE, 2009, pp. 1–6.

- [14] F. Alonso-Fernandez, J. Bigun, A survey on periocular biometrics research, *Pattern Recognition Letters* 82 (2016) 92–105.
- [15] L. C. O. Tiong, Y. Lee, A. B. J. Teoh, Periocular recognition in the wild: Implementation of rgb-oclbcp dual-stream cnn, *Applied Sciences* 9 (13) (2019) 2709.
- [16] K. Hernandez-Diaz, F. Alonso-Fernandez, J. Bigun, One-shot learning for periocular recognition: Exploring the effect of domain adaptation and data bias on deep representations, *IEEE Access* (2023).
- [17] J. Bigun, *Vision with Direction*, Springer, Heidelberg, 2006. doi:10.1007/b138918.
- [18] J. Bigun, G. Granlund, Optimal orientation detection of linear symmetry, in: *First ICCV*, London, June 8–11, IEEE Computer Society, 1987, pp. 433–438.
- [19] J. Weickert, Coherence-enhancing diffusion filtering, *International journal of computer vision* 31 (1999) 111–127.
- [20] F. Szczepankiewicz, D. van Westen, E. Englund, C.-F. Westin, F. Ståhlberg, J. Lätt, P. C. Sundgren, M. Nilsson, The link between diffusion mri and tumor heterogeneity: Mapping cell eccentricity and density by diffusional variance decomposition (divide), *Neuroimage* 142 (2016) 522–532.

- [21] T. Lindeberg, Scale-space theory in computer vision, Vol. 256, Springer Science & Business Media, 2013.
- [22] K. Mikolajczyk, C. Schmid, Scale & affine invariant interest point detectors, *International journal of computer vision* 60 (1) (2004) 63–86.
- [23] A. Bruhn, J. Weickert, C. Schnörr, Lucas/kanade meets horn/schunck: Combining local and global optic flow methods, *International Journal of Computer Vision* 61 (3) (2005) 211–231.
- [24] X. Si, J. Feng, B. Yuan, J. Zhou, Dense registration of fingerprints, *Pattern Recognition* 63 (2017) 87–101.
- [25] A. Mikaelyan, F. Alonso-Fernandez, J. Bigun, Keypoint description by symmetry assessment – applications in biometrics (2023). [arXiv:2311.01651](https://arxiv.org/abs/2311.01651).
- [26] A. Alekseev, A. Bobe, Gabornet: Gabor filters with learnable parameters in deep convolutional neural network, in: 2019 International Conference on Engineering and Telecommunication (EnT), IEEE, 2019, pp. 1–4.
- [27] R. P. Singh, R. Dash, R. K. Mohapatra, Lbp and cnn feature fusion for face anti-spoofing, *Pattern Analysis and Applications* 26 (2) (2023) 773–782.
- [28] F. Juefei-Xu, V. Naresh Boddeti, M. Savvides, Local binary convolu-

- tional neural networks, in: Proceedings of the IEEE conference on computer vision and pattern recognition, 2017, pp. 19–28.
- [29] L. Kalake, Y. Dong, W. Wan, L. Hou, Enhancing detection quality rate with a combined hog and cnn for real-time multiple object tracking across non-overlapping multiple cameras, *Sensors* 22 (6) (2022) 2123.
- [30] P. Kumari, K. Seeja, A novel periocular biometrics solution for authentication during covid-19 pandemic situation, *Journal of Ambient Intelligence and Humanized Computing* 12 (2021) 10321–10337.
- [31] X. Pan, Fusing hog and convolutional neural network spatial–temporal features for video-based facial expression recognition, *IET Image Processing* 14 (1) (2020) 176–182.
- [32] J. Y. Choi, B. Lee, Ensemble of deep convolutional neural networks with gabor face representations for face recognition, *IEEE Transactions on Image Processing* 29 (2019) 3270–3281.
- [33] M. M. T. Zadeh, M. Imani, B. Majidi, Fast facial emotion recognition using convolutional neural networks and gabor filters, in: 2019 5th Conference on Knowledge Based Engineering and Innovation (KBEI), IEEE, 2019, pp. 577–581.
- [34] S. Hosseini, N. I. Cho, Gf-capsnet: Using gabor jet and capsule networks for facial age, gender, and expression recognition, in: 2019 14th IEEE

- International Conference on Automatic Face & Gesture Recognition (FG 2019), IEEE, 2019, pp. 1–8.
- [35] K. He, X. Zhang, S. Ren, J. Sun, Deep residual learning for image recognition, in: Proceedings of the IEEE conference on computer vision and pattern recognition, 2016, pp. 770–778.
- [36] G. Huang, Z. Liu, L. Van Der Maaten, K. Q. Weinberger, Densely connected convolutional networks, in: Proceedings of the IEEE conference on computer vision and pattern recognition, 2017, pp. 4700–4708.
- [37] F. Chollet, Xception: Deep learning with depthwise separable convolutions, in: Proceedings of the IEEE conference on computer vision and pattern recognition, 2017, pp. 1251–1258.
- [38] C. Szegedy, V. Vanhoucke, S. Ioffe, J. Shlens, Z. Wojna, Rethinking the inception architecture for computer vision, in: Proceedings of the IEEE conference on computer vision and pattern recognition, 2016, pp. 2818–2826.
- [39] M. Sandler, A. Howard, M. Zhu, A. Zhmoginov, L.-C. Chen, Mobilenetv2: Inverted residuals and linear bottlenecks, in: Proceedings of the IEEE conference on computer vision and pattern recognition, 2018, pp. 4510–4520.
- [40] L. A. Zanolensi, D. R. Lucio, A. d. S. Britto Junior, H. Proença,

- D. Menotti, Deep representations for cross-spectral ocular biometrics, *IET Biometrics* 9 (2) (2020) 68–77.
- [41] A. Sequeira, L. Chen, P. Wild, J. Ferryman, F. Alonso-Fernandez, K. B. Raja, R. Raghavendra, C. Busch, J. Bigun, Cross-eyed-cross-spectral iris/periocular recognition database and competition, in: 2016 International Conference of the Biometrics Special Interest Group (BIOSIG), IEEE, 2016, pp. 1–5.
- [42] P. R. Nalla, A. Kumar, Toward more accurate iris recognition using cross-spectral matching, *IEEE transactions on Image processing* 26 (1) (2016) 208–221.
- [43] P. K. A. Vasu, J. Gabriel, J. Zhu, O. Tuzel, A. Ranjan, Fastvit: A fast hybrid vision transformer using structural reparameterization, in: *Proceedings of the IEEE/CVF International Conference on Computer Vision*, 2023.
- [44] Y. Mo, Y. Wu, X. Yang, F. Liu, Y. Liao, Review the state-of-the-art technologies of semantic segmentation based on deep learning, *Neurocomputing* 493 (2022) 626–646.
- [45] L. Yang, Z. Zhang, Y. Song, S. Hong, R. Xu, Y. Zhao, W. Zhang, B. Cui, M.-H. Yang, Diffusion models: A comprehensive survey of methods and applications, *ACM Computing Surveys* 56 (4) (2023) 1–39.